hydrology

MDPI

Article

Hydrodynamic Parameter Estimation for Simulating Soil-Vegetation-Atmosphere Hydrology Across Forest Stands in the Strengbach Catchment

Benjamin Belfort *, Aya Alzein, Solenn Cotel, Anthony Julien and Sylvain Weill

ITES (Institut Terre et Environnement de Strasbourg), University of Strasbourg, ITES UMR 7063, F-67084 Strasbourg, France; alzein@unistra.fr (A.A.); cotel@unistra.fr (S.C.); anthony.julien@unistra.fr (A.J.); s.weill@unistra.fr (S.W.)

* Correspondence: belfort@unistra.fr

Abstract

Modeling the water cycle in the critical zone requires understanding interactions between the soil–vegetation–atmosphere compartments. Mechanistic modeling of soil water flow relies on the accurate determination of hydrodynamic parameters that control hydraulic conductivity and water retention curves. These parameters can be derived either using pedotransfer functions (PTFs), using soil properties obtained from field samples, or through inverse modeling, which allows the parameters to be adjusted to minimize differences between simulations and observations. While PTFs are widely used due to their simplicity, inverse modeling requires specific instrumentation and advanced numerical tools. This study, conducted at the Hydro-Geochemical Environmental Observatory (Strengbach forested catchment) in France, aims to determine the optimal hydrodynamic parameters for two contrasting forest plots, one dominated by spruce and the other by beech. The methodology integrates granulometric data across multiple soil layers to estimate soil parameters using PTFs (Rosetta). Water content and conductivity data were then corrected to account for soil stoniness, improving the KGE and NSE metrics. Finally, inverse parameter estimation based on water content measurements allowed for refinement of the evaluation of α, Ks, and n. This framework to estimate soil parameter was applied on different time periods to investigate the influence of the calibration chronicles on the estimated parameters. Results indicate that our methodology is efficient and that the optimal calibration period does not correspond to one with the most severe drought conditions; instead, a balanced time series including both wet and dry phases is preferable. Our findings also emphasize that KGE and NSE must be interpreted with caution, and that long simulation periods are essential for evaluating parameter robustness.

Keywords: soil-plant-atmosphere modeling; forest ecosystem; hydrodynamic parameters; inverse estimation

Check for updates

Academic Editor: Yafeng Zhang

Received: 17 November 2025
Revised: 19 December 2025
Accepted: 22 December 2025
Published: 24 December 2025

Copyright: © 2025 by the authors. Licensee MDPI, Basel, Switzerland. This article is an open access article distributed under the terms and conditions of the Creative Commons Attribution (CC BY) license.

1. Introduction

Bibliometric analyses reveal a growing interest in the study of forest ecosystems, likely reflecting the increasing challenges they face [1]. Indeed, on the one hand, forests provide a wide range of ecosystem services, including food production, timber and fuel supply, water conservation and regulation, carbon sequestration, biodiversity protection, climate regulation, as well as ecotourism and other recreation activities [2]. However,

their long-term sustainability is increasingly threatened by multiple anthropogenic pressures, particularly the expansion of agricultural lands and urban areas, along with the adverse impacts of climate change (CC) [3]. CC, in turn, manifests through prolonged droughts, disruptions in water availability, soil erosion, and declining soil fertility, factors that collectively weaken forest ecosystems, reduce their capacity to withstand and recover from such perturbations [3,4], and ultimately increase global tree mortality [5]. One the other hand, a combination of interacting factors is at play: for instance, the more frequent droughts observed over the past decade have not only caused water shortages and induced physiological stress in trees, but have also triggered indirect damage through pest outbreaks—most notably bark beetle infestations [6]—and increased the risk of large-scale fires [7].

Water is a key component to understanding ecosystem functioning. Its circulation and the complex interactions within the soil–tree–atmosphere continuum are central concerns in ecohydrology. While climate and soil moisture regulate vegetation dynamics, forest ecosystems also strongly influence the overall water balance and generate multiple feedback loops [8]. Hence, soil moisture and vapor pressure deficit appear among the most influential factors controlling forest water use [9].

Characterizing the spatial and temporal dynamics of water storage in soils is therefore essential. This need has, for instance, motivated the development of large-scale soil moisture monitoring databases [10] and efficient treatment of satellite-based measurements [11]. Ground-based observation networks, focusing on the critical zone and supporting interdisciplinary research, continue to play a crucial role in the development and validation of such approaches [12,13]. Moreover, many studies—particularly those with predictive objectives related to water resources under CC—rely on models in which hydrodynamic properties must be accurately defined [14,15]. With advances in computational material and methods, subsurface and groundwater flows are now widely represented in hydrological models using the Richards' equation, particularly when applied at the catchment scale [14–17]. The hydrodynamic parameters used to describe the water retention and hydraulic conductivity curves of porous media can be estimated through pedotransfer functions (PTFs), which are generally derived from particle-size analyses of soil samples [14,18,19]. Other approaches based on geophysical measurements can also be considered to characterize subsurface structures and properties in a less intrusive manner and/or to cover a larger spatial extent [20,21]. When soil moisture or drainage data are recorded in situ (e.g., TDR sensors and/or lysimeters), it becomes possible to relate hydrodynamic parameters to time series through an inverse modeling approach. Although such methods require numerical expertise and measurement efforts that can be complex due to field constraints, they nevertheless yield valuable and insightful results [19,22]. The presence of rock fragments in the soil is often overlooked, as most hydrodynamic models are not designed to account for their influence. Nevertheless, introducing appropriate corrections may be essential to accurately evaluate water dynamics and storage in porous media [23,24].

A study conducted at the Strengbach catchment Observatory (Vosges Mountains, France) investigated the impact of monitoring frequency on the estimation of soil hydrodynamic parameters and proposed a consistent parameter set derived from matric potential measurements along a vertical soil profile [22]. Although earlier studies showed that daily data were sufficient, we opted for hourly WC measurements to capture rapid hydrological variations, particularly in the context of drought and recharge events observed during the recent study period, which had not been considered until now.

The primary objective of the present study is to present a methodology to derive relevant soil parameters from mixing PFTs and inverse modeling approaches in order to propose sets of hydrodynamic parameters suitable for hydrological modeling within the

forested Strengbach catchment. These parameters are derived for two long-term monitoring plots, respectively dominated by spruce (*Picea abies*) and beech (*Fagus sylvatica*). The original results presented here are based on soil water content measurements obtained from two vertical profiles where soil samples were collected and analyzed. The conventional approach based on PTFs is refined to explicitly account for the influence of soil stoniness, thereby improving the representativeness of the derived hydrodynamic properties. Although illustrated here for the Strengbach catchment, this methodology is not site-specific and can be applied to other mountainous regions or sites with soils containing coarse fragments and stones.

2. Materials and Methods

The following sections successively present the study site and characteristics of the two plots studied. The instruments used for data acquisition are then described, along with the classical estimation of the hydrodynamic parameters based on granulometry. In sequence, the calculation of potential evapotranspiration and its implementation in the BILHYDAY model contribute to the estimation of actual evapotranspiration (AET). This variable is involved in defining the upper boundary condition used in the inverse modeling approach based on Richards' equation, which is also presented. Finally, a specific section details the methodological aspects necessary to understand the steps involved in parameter estimation.

2.1. General Description of the Site

The Strengbach research catchment is located in the high-altitude commune of Aubure (Vosges Mountains, Haut-Rhin, France, see Figure 1). This experimental site covers an area of 0.8 km^2 and extends from 850 to 1150 m a.s.l. Approximately 80% of the catchment is forested, with about 76% consisting of a monospecific Norway spruce (*Picea abies*) plantation and the remaining area dominated by beech (*Fagus sylvatica*) [25]. Following severe forest dieback, largely attributed to pest outbreaks, the spruce stand at this site was completely clear-cut, and new monitoring systems were installed in 2022 on two more resilient plots. From a pedological perspective, the catchment is characterized by acidic brown and ochreous podzolic soils developed on a calcium-poor granitic substrate [25]. Over the past 18 years (2007–2025), mean annual precipitation was 1223 mm, mean annual temperature 6.7 °C, and total potential evapotranspiration (PET) 586 mm.

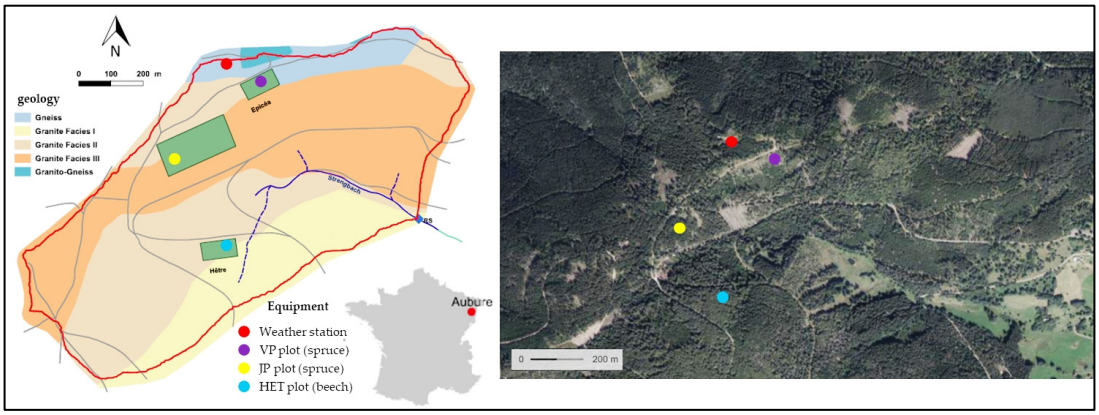


Figure 1. Location of the Strengbach catchment in the Grand-Est region, France, showing the geological facies map and the position of the main monitoring equipment. The aerial view on the right, extracted from the Geoportail website (@IGN), dates from 2024 and provides an overview of the vegetation cover.

Meteorological, hydrological, and geochemical variables of the Strengbach catchment have been continuously monitored since 1986 by the Hydro-Geochemical Environmental Observatory (OHGE; https://ohge.unistra.fr, accessed on 23 December 2025). The initial establishment of the monitoring network was motivated by research on acid rain and its effects on forest ecosystems. Current investigations now address a wider range of environmental issues, including forest decline associated with nutrient-poor soils [26,27], the impacts of climate change [28], and water resource management [29,30]. In addition, methodological developments are being pursued to improve the characterization of subsurface aquifers throughout multidisciplinary research [20,25,31].

2.2. Monitoring Devices and Associated Measurements

The Strengbach catchment is equipped with a meteorological station located in an open area at the top of the mountain (cf. Figure 1). Precipitation is measured using a tipping-bucket rain gauge (model R5-302 b, Précis Mécanique, Bezons, France). Air temperature and relative humidity are recorded at a height of 1.5 m with a Vaisala HMP45C probe (Vaisala Oyj, Vantaa, Finland). Wind speed and direction are measured with an R.M. Young anemometer (model 05103, R.M. Young Company, Traverse City, MI, USA), and incoming global radiation is monitored using a Kipp & Zonen pyranometer (model CM6B, Kipp & Zonen B.V., Delft, the Netherlands). All measurements are recorded by a Campbell CR1000X datalogger (Campbell Scientific Inc., Logan, UT, USA) at a 10 min time step.

For soil moisture monitoring, in the spruce plot (denoted JP in Figure 1), a soil pit was excavated to install Campbell TDR probes (model CS616, Campbell Scientific Inc., Logan, UT, USA) at depths of 13, 31, 52, 72, and 92 cm. In addition, four Campbell temperature probes (model 107, Campbell Scientific Inc., Logan, UT, USA) were installed at the first four depths to enable temperature correction. The sensor raw period (τ_{raw}, in µs) was corrected using a quadratic function of soil temperature (T_{soil}, in °C), defined in Equation (1):

$$\tau_{cor} = \tau_{raw} + (20 - T_{soil}) \times \left(5.26 \times 10^{-1} - 5.2 \times 10^{-2} \times \tau_{raw} + 1.36 \times 10^{-3} \times {\tau_{raw}}^2\right) \quad (1)$$

Following several laboratory calibration tests conducted on soil samples of the Strengbach catchment, the standard quadratic calibration equation provided by the manufacturer was retained to derive the volumetric water content (θ, in m^3/m^3), as shown in Equation (2):

$$\theta = -6.63 \times 10^{-2} - 6.3 \times 10^{-3} \times \tau + 7 \times 10^{-4} \times \tau^2 \quad (2)$$

Notice that the manufacturer indicates a stated error of about 2.5% and 1.5%, for the TDR-CS616 probe and the SoilVue10 (described later), respectively, which combines with the calibration error and the biases induced by imperfect installation. Few studies have evaluated the impact of calibration of such water content sensors in forest soils [32], yet it is far from negligible, especially in topsoils (0.16 m^3/m^3 mentioned in [32]). In the case of coarse-textured soils, this effect is certainly less pronounced [33]. The underestimation that may occur [32] is also difficult to assess in contexts with stony soils, since direct in situ measurements are challenging and, in our case, were only performed during the installation phase, when the soil pit remained open.

In the beech plot (denoted HET in Figure 1), a 50 cm Campbell SoilVue10 probe (Campbell Scientific Inc., Logan, UT, USA) was installed, providing measurements of volumetric water content at depths of 5, 10, 20, 30, 40, and 50 cm. This sensor internally applies the correction and calibration equations and directly reports the volumetric water content. For both plots, WC data were recorded every 10 min on Campbell CR1000 (JP) and CR1000X (HET) dataloggers.

Notice that the SoilVue10 sensor was installed by inserting the probe into a 50 cm deep auger-drilled hole, without the need for pit excavation. Due to the pedological characteristics of the stand, a certain period of time was necessary for proper soil–probe contact to be established. A preliminary data processing step was applied to filter out measurements affected by preferential flow along the vertical probe and by water accumulation at the bottom of the hole. It should also be noted that this device operates at shallower depths and does not rely on exactly the same type of sensors as the installation on the JP stand.

Although these data were primarily used as input for the inverse modeling process, the precipitation and soil moisture time series are presented in the Results section to enhance the comprehension and assessment of the modeling outcomes. A complementary hydrological analysis is also provided.

2.3. Vertical Profiles and Soil Properties

Samples were collected in April 2022 from the JP plot at eleven depths (Figure 2a). Soil composition was determined using a laser diffraction particle sizing technique. The soil was mainly composed of particles larger than 2 µm, corresponding to sand and loam fractions, with the latter generally more abundant, averaging 53% compared to 35% for the sand fraction. For the HET plot (Figure 2b), data from [26] were used. These were based on the same analytical technique and showed that the sand fraction is dominant, exceeding 59% across the depths analyzed, with a mean value of 65%, compared to 24% and 11% for the loam and clay fractions, respectively. From a practical perspective, the characterization of the spruce plot relied solely on the samples collected from the pit used for sensor installation. For the beech plot, the granulometric data were derived from averages based on five vertical profiles. Given the conditions under which the probe was installed at this site, it was not feasible to obtain a characterization exactly at the installation location.

Sensor locations are shown in Figure 2a,b (red stars on the right side). Due to restrictions on operating the devices and the complexity of parameter estimation under natural conditions, the domain discretization was simplified. A step in our methodology described in Section 2.5 consists of selecting relatively homogeneous layers, each containing at least one sensor, and estimating their hydrodynamic parameters. Figure 2c,d shows the pit excavated for sensor installation and sampling, with visible coarse elements that were not captured by the soil sampling cylinders of approximately 4 cm radius. The site was refilled while maintaining the original sequence of soil layers as much as possible, in order to monitor moisture dynamics in an environment minimally disturbed given the chosen methodology.

(**a**)

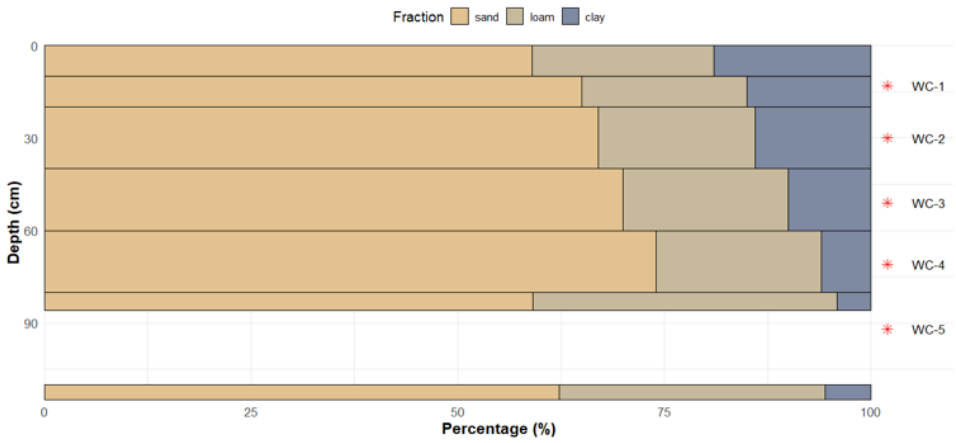


Figure 2. *Cont.*

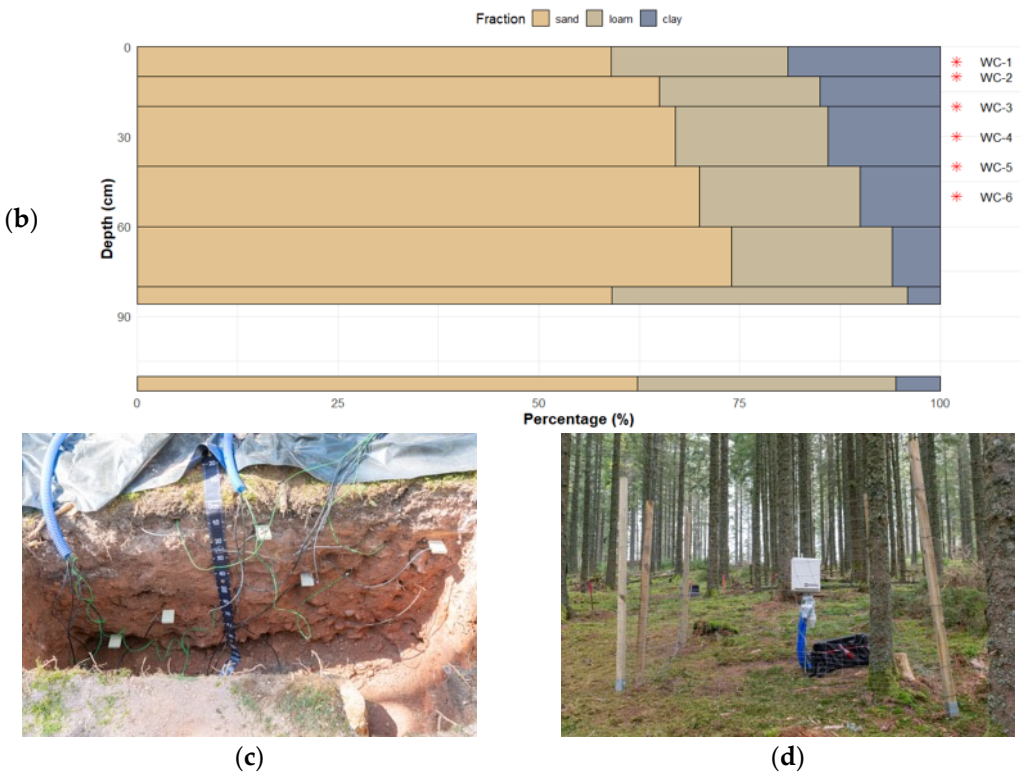


Figure 2. (**a**,**b**) Soil composition profiles obtained from disturbed samples for the JP and HET plots, respectively; red stars indicate WC measurements. (**c**) Photograph of the pit and sensors before refilling in the JP plot (April 2022). (**d**) Photograph of JP soil data monitoring after refilling (April 2022).

2.4. Numerical Methods

2.4.1. Potential and Actual Evapotranspiration

The choice of the potential evapotranspiration (PET) estimation method is crucial for accurately quantifying water fluxes in hydrological models [34]. To ensure consistency with previous studies conducted in the Strengbach watershed [22,35], the formulation derived from the Penman equation by Brochet and Gerbier [36] was adopted, as presented in Equation (3). Earlier studies have demonstrated that this approach accounts for the specific characteristics of the experimental site, particularly in the computation of net radiation in the radiative term (first component on the r.-h. s. term of Equation (3)) and in the formulation of the advective term (second component on r.-h. s. term of Equation (3)).

$$PET_{BG} = \frac{1}{59}\frac{\Delta R_n}{(\Delta+\gamma)} + \frac{\gamma}{(\Delta+\gamma)}0.26 \times (1 + 0.4 \times u_{10})\delta_e \quad (3)$$

PET_{BG} is given in $mm.d^{-1}$, Δ is the derivative of saturated vapor pressure versus temperature ($mbar.K^{-1}$) expressed as the air temperature Ta (°C) (see Equation (4)), R_n is the net radiation at the canopy surface ($cal.cm^{-2}.d^{-1}$), δ_e is the saturation vapor pressure deficit (mbar) expressed at the air temperature T_a (°C) and the relative humidity H_r (%) (see Equation (5)), γ is the psychrometric constant (0.66 $mbar.K^{-1}$) and u_{10} is the adjusted wind speed at 10 m height ($m.s^{-1}$).

$$\Delta = \frac{25,039}{(237.3 + T_a)^2} \cdot 10^{\frac{7.5 \times T_a}{237.3+T_a}} \quad (4)$$

$$\delta_e = (1 - H_r) \times 6.107 \times 10^{\frac{7.5 \times T_a}{237.3+T_a}} \quad (5)$$

Originally, the estimation of net radiation was derived from measurements of global radiation, complemented by a sunshine duration table used for potential corrections. Consequently, the preceding equations (Equations (3)–(5)) enabled the calculation of the daily PET_{BG}. Nevertheless, since meteorological measurements are available at a higher frequency, PET can also be estimated at an hourly resolution (notice that daily and hourly values have been used in this study).

If PET represents the maximum evapotranspiration under well-watered conditions, the actual evapotranspiration (AET) accounts for water stress as well as precipitation intercepted and subsequently evaporated by vegetation foliage throughout the different seasons. An in-house code, BILHYDAY, based on a daily water mass balance and following a conceptual approach (see principles in [37]), was used to estimate AET according to Equation (6):

$$AET = Tr + In + SEvap \quad (6)$$

where Tr refers to transpiration by the canopy ($mm.d^{-1}$), In is the interception ($mm.d^{-1}$), and SEvap is the soil and understory evaporation ($mm.d^{-1}$).

Meteorological variables such as wind velocity, net radiation, air temperature, relative humidity, and recorded precipitation are provided to BILHYDAY as input data, along with site-specific parameters describing the canopy, plant interception, soil evaporation, and ecophysiological characteristics. PET_{BG} is then computed, and the three components of AET in Equation (6) are partly driven by the maximum leaf area index (LAI), a dimensionless variable that characterizes plant canopies and is defined as the projected leaf area per unit ground area. Since runoff has never been observed at the experimental site due to the continuous vegetation cover, the BILHYDAY model is well suited for estimating AET on a daily time step and has previously been calibrated on different plots of our research catchment [35,38]. The AET time series used to define the upper boundary condition are described in the Results section. In summary, BILHYDAY is employed as a pre-processing tool to supply WAMOS-IPE-1D, on a plot-specific basis, with surface flux inputs that encapsulate soil–tree–atmosphere interactions (see Section S2 of the Supplementary Materials for details). It should be noted that the primary focus of the present study lies in the parametrization of subsurface water flow within the soil, as presented in the following paragraphs.

2.4.2. Vadose Zone Model

The adopted hydrological model is based on Richards' equation (Equation (7)) [39], which results from the combination of the mass conservation equation and the Darcy–Buckingham law, and describes water movement in a variably saturated porous medium.

$$\frac{\partial \theta}{\partial t} + S\frac{\theta}{\theta_s}\frac{\partial h}{\partial t} = \frac{\partial}{\partial z}\left[K(h)\left(\frac{\partial h}{\partial z} - 1\right)\right] \quad (7)$$

where S is the storage coefficient (m^{-1}), θ is the volumetric water content ($m^3.m^{-3}$), θ_s is the saturated water content ($m^3.m^{-3}$), h is the pressure head (m), z is the vertical distance positive downward (m), t is the time (d), and K is the hydraulic conductivity ($m.d^{-1}$).

In addition, the standard Mualem–van Genuchten (MvG) model (Equations (8) and (9)) [40,41] defines the relationships between negative pressure head, water content, and relative hydraulic conductivity (K_r, $m.d^{-1}$).

$$S_e = \frac{\theta - \theta_r}{\theta_s - \theta_r} = \left[1 + (\alpha|h|)^n\right]^{-m} \quad (8)$$

$$K(S_e) = K_{sat} \times K_r(S_e) = K_{sat} \times S_e{}^L\left[1 - \left(1 - (S_e)^{1/m}\right)^m\right]^2 \quad (9)$$

where S_e is the effective saturation (-), θ_r is the residual water content ($m^3.m^{-3}$), α is a parameter related to the mean pore size (m^{-1}), n is a parameter reflecting the uniformity of the pore size distribution (-), m = 1–1/n is a parameter (-) [41], K_{sat} is the saturated hydraulic conductivity ($m.d^{-1}$), and L is a parameter related to the tortuosity chosen here equal to 0.5 (-) [40]. Notice that for saturated conditions (i.e., $h \geq 0$), $K = K_{sat}$ and $S_e = 1$.

The vertical profiles of forest soils contain a non-negligible proportion of stones and coarse fragments, which are generally not represented in samples collected and analyzed in the laboratory. To account for their effect on the evaluation of flow in the vadose zone, a corrective model for water content and hydraulic conductivity was implemented [23]. This model consists of two Equations (10) and (11) for the water content and hydraulic conductivity, respectively [23,24,42,43].

$$\theta^b = (1 - R_v)\theta^f \quad (10)$$

$$K_{sat}^b = (1 - a \times R_v)K_{sat}^f \quad (11)$$

It is important to note that coarse fragments strongly affect soil hydraulic behavior—altering pore connectivity, effective pore volume, preferential flow paths, and hydraulic conductivity—and readers can consult several studies for further details [23,24,42,43].

In Equations (10) and (11), the subscript b denotes the bulk value, whereas f refers to the fine soil fraction. The parameter a represents the hydraulic resistance of rock fragments to water flow and depends on their shape and size (-), while R_v denotes the relative volumetric fraction of stones ($cm^3.cm^{-3}$). The parameter a was set to 1.1 in accordance with [43], while the coefficient R_v was adjusted according to the plot and soil layer in question.

Hence, a set of 5 parameters (K_{sat}, θ_s, θ_r, n, α) is needed for each layer of the considered domain. Finally, the model requires specification of the upper and lower boundary conditions throughout the simulation period.

2.4.3. Simulations Achieved

Simulations for the period 2022–2025 were performed using WaMoS-IPE-1D (Water Movement in Soil-Inverse Parameter Estimation-1D), respectively for the spruce and beech plots. The numerical methods implemented in this Fortran code to solve Richards' equation (Equation (7)) include: (i) a finite element method for spatial discretization; (ii) a fully implicit backward Euler scheme for temporal integration; (iii) a variable switching approach employing modified Picard or Newton methods for linearization [44]; (iv) a heuristic time-stepping strategy based on iteration counts [45]; (v) a switching, flux-controlled procedure for the top boundary condition to maintain physically realistic results [46]; and (vi) a Levenberg–Marquardt iterative algorithm to solve the inverse problem [47]. A detailed description of the code is provided in Lehmann and Ackerer [48]. For more details on the inverse modeling approach in general, the reader is referred to [49].

A uniform 1 cm mesh was adopted for the spatial discretization of both vertical profiles. Simulations were initialized with a specified hydrostatic pressure head profile derived from the lower water content measurement and allowed a sufficiently long warm-up period to ensure that initial conditions did not influence parameter estimation. An imposed flux boundary condition was applied at the soil surface, while the bottom boundary was defined as free drainage. As mentioned in Section 2.4.1, the BILHYDAY code allows for the estimation of daily AET, which is then converted to hourly AET using Equation (12). The top boundary condition is subsequently imposed at an hourly time step by subtracting the hourly AET from the rainfall.

$$AET_h = \frac{PET_{BG,h}}{PET_{BG,day}} AET_{day} \quad (12)$$

2.5. Methodology Investigated for the Model Calibration

The proposed methodology consists of the following steps:

1. Definition of homogeneous soil layers
   The first step consisted of subdividing the soil profile into homogeneous layers, each containing at least one sensor. Two different configurations to describe the 110 cm deep profile in the JP stand were set, while only one was used for the 100 cm deep HET profile.
2. Initialization of hydrodynamic parameters
   Field sampling and subsequent laboratory analyses enabled the determination of soil texture and composition for the different configurations described previously. Table 1 presents the configurations for the JP and HET stands. Although the uncertainty associated with the granulometric measurements was not provided, standard deviations are reported in Table 1, as the layer characterization was based on the aggregation of multiple samples. Following [22], initial estimates of the soil hydraulic parameters were obtained using the ROSETTA software based on PTFs [18], which derives parameters from measured soil texture data (Rosetta 1, https://www.handbook60.org/rosetta/, accessed on 10 March 2025).
3. Adjustments to account for stoniness
   The granulometric analyses performed on disturbed soil samples were considered representative of the fine soil fraction. In contrast, both simulated and measured water contents represent the global bulk soil response. Consequently, the initial hydraulic parameters were corrected using the volumetric stone fraction (R_v) reported in Table 1 to account for the influence of stoniness on the soil water dynamics and the referring properties detailed in Equations (10) and (11).
4. Calibration and validation simulations
   Given the available measurement ranges (which differ between the two sites), parameter inverse estimation was conducted using the WaMoS-IPE-1D model. The optimization procedure minimized an objective function defined as the mean squared error between observed and simulated water contents (θ_{meas} and θ_{sim}, respectively):

$$Er = \sum_{n=1}^{N_{time}} \sum_{i=1}^{N_{sens}} \left(\theta^n_{sim,i} - \theta^n_{meas,i}\right)^2 \quad (13)$$

where N_{time} is the number of observation times and N_{sens} denotes the number of layers instrumented with a sensor and used for the calibration.

Table 1. Soil composition for the various configurations tested at the JP and HET plots, along with the relative stone volume fraction for each configuration. Where applicable, standard deviations are reported in parentheses.

Config.	Layer Min–Max Depth (cm)	Clay (%)	Loam (%)	Sand (%)	R_v (−)
JP-1	0–40	10.25 (±1.65)	51.81 (±7.08)	37.94 (±8.51)	0
	40–75	10.62 (±2.50)	48.61 (±11.33)	40.77 (±13.83)	0.1
	75–110	12.75	61.52	25.73	0.5
JP-2	0–35	10.25 (±1.65)	51.81 (±7.08)	37.94 (±8.51)	0
	35–65	9.77 (±2.84)	44.65 (±12.76)	45.58 (±15.61)	0.1
	65–110	12.54 (±0.30)	59.02 (±3.53)	28.44 (±3.83)	0.2
HET-1	0–25	17 (±2.83)	21 (±1.41)	62 (±4.24)	0.1
	25–45	14	19	67	0.2
	45–100	10 (±3.01)	25.6 (±9.70)	67.7 (7.71)	0.4

Following [22], the inverse modeling approach focused on optimizing three key parameters: the saturated hydraulic conductivity (K_{sat}), the shape parameter (α), and the pore-size distribution index (n). Hence, on the one hand, applying Equation (10) is really important to obtain a proper estimation of θ_r and θ_s that are not estimated by our inverse model. On the other hand, K_{sat} will be optimized and Equation (11) is only useful for initialization. The quality of the calibrated parameter set was subsequently assessed using the Kling–Gupta Efficiency criterion [50] computed over the overall period of measurements according to Equation (14):

$$KGE = 1 - \sqrt{(r-1)^2 + (\alpha-1)^2 + (\beta-1)^2} \quad (14)$$

where r refers to the correlation coefficient between the simulated and observed WC, α to the ratio of their standard deviations, and β to the ratio of their mean values.

The Nash–Sutcliffe Efficiency (NSE) criterion [51] given in Equation (13) can also be computed:

$$SE = 1 - \frac{\sum_{n=1}^{N_{time}} \sum_{i=1}^{N_{sens}} \left(\theta^n_{sim,i} - \theta^n_{meas,i}\right)^2}{\sum_{n=1}^{N_{time}} \sum_{i=1}^{N_{sens}} \left(\overline{\theta_i} - \theta^n_{meas,i}\right)^2} \quad (15)$$

where $\overline{\theta_i}$ refers to the mean volumetric water content of the ith layer over the period of concern. KGE and NSE values approaching 1 reflect an excellent agreement between the simulated and observed data, while negative values indicate that the model performs with lower accuracy compared to the mean of the observations as a predictor.

Depending on the plot considered (with different data availability), four calibration periods were selected:

- Calib.1: from 1 May 2022 to 30 September 2022 (no data available for HET),
- Calib.2: from 1 April 2023 to 31 December 2023,
- Calib.3: from 1 April 2024 to 31 December 2024,
- Calib.4: from 1 October 2024 to 30 September 2025.

One objective of the present study was to investigate the impact of the period used for calibration on the estimation of the parameters. The rest of the period was used for the validation step.

3. Results

This section is dedicated to (i) the presentation of the meteorological time series and to the estimation of the mean site-scale potential evapotranspiration (PET), and (ii) the presentation of the results obtained for each plot (JP and HET, respectively) regarding the imposed upper boundary conditions and the outcomes of the parameter estimation using the inverse modeling approach.

3.1. Time Series of Climatic Forcing and PET

Meteorological data for the period of interest are presented in Figure 3. The hydrological year Y runs from 1 October of year Y to 30 September of year Y + 1. The temporal evolution of daily precipitation and mean air temperature was used in the model described in Section 2.4.1 to estimate potential evapotranspiration (PET). The four hydrological years considered exhibited substantial inter-annual variability relative to the 18-year climatological mean. The 2021 hydrological year, characterized by the summer drought of 2022, was the driest of the past 18 years (−20.7% rainfall, +18.8% PET relative to the long-term average), whereas 2023 was the wettest (+32% rainfall, −3.3% PET relative to the long-term average). Figures S1 and S2 illustrate this meteorological variability.

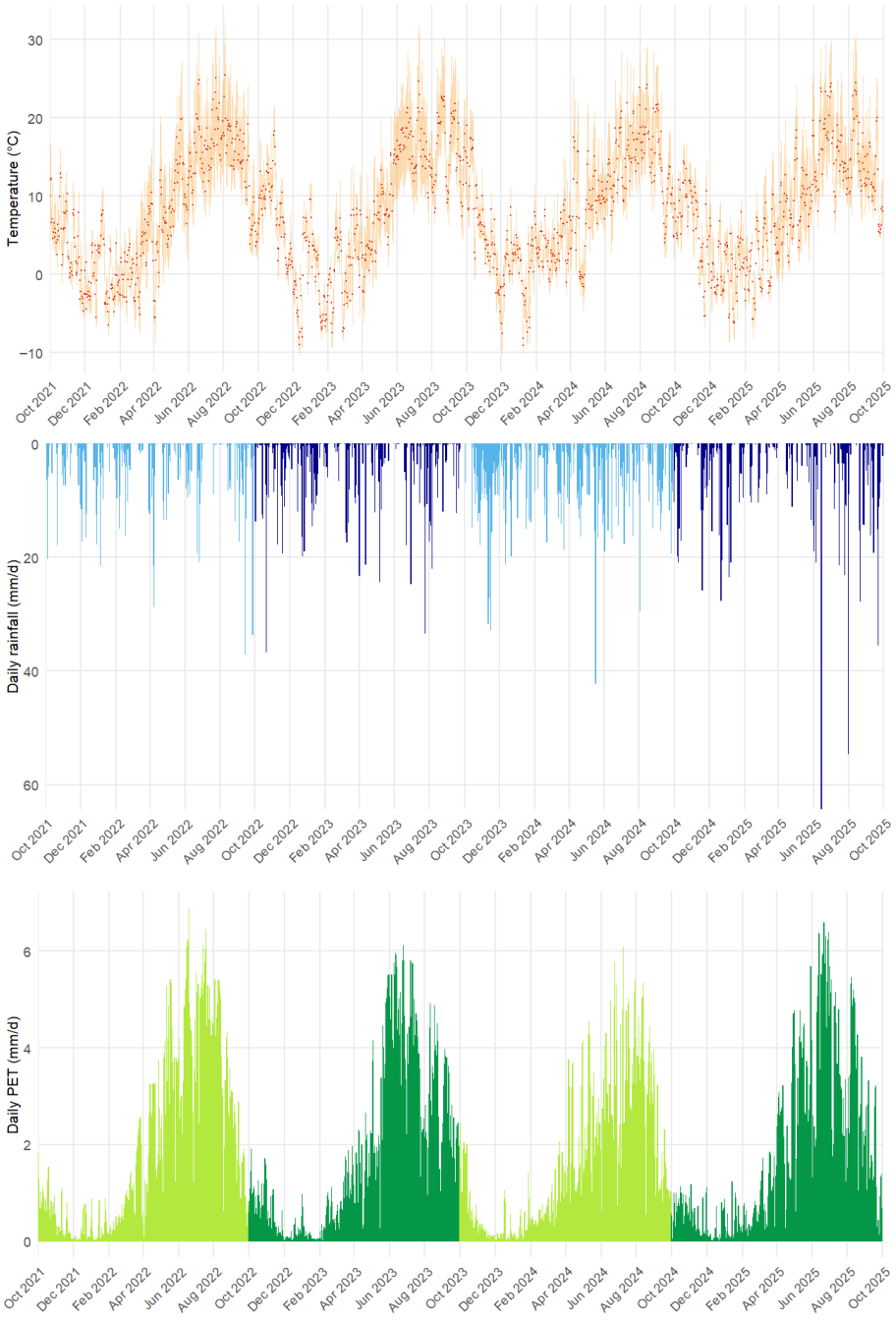


Figure 3. Daily meteorological variables for the four hydrological years 2021–2024 (1 October of year Y to 30 September of year Y + 1); (**a**) mean daily temperature (red marks) with the daily minimum–maximum range shown in orange; (**b**) daily precipitation; (**c**) potential evapotranspiration (PET) estimated from Equation (3). The alternating light and dark green shading indicates successive hydrological years.

3.2. Results at JP Plot

Equation (12) was used to compute the AET at an hourly time step (based on BILHY-DAY outputs). The resulting flux, used as a BC at the soil surface in the Wamos-IPE-1D model, corresponds to the difference between incoming precipitation and AET, as shown in Figure 4a. As commonly observed, the flux is positive, indicating a net meteoric water input to the soil. However, at the seasonal scale, the situation is more contrasted: AET accounts for between 44% and 86% (for the 2023 and 2024 hydrological years, respectively) of precipitation during the spring season (April–June), and between 57% and nearly 75%

(for the 2023 and 2022 hydrological years, respectively) of precipitation during summer (July–September).

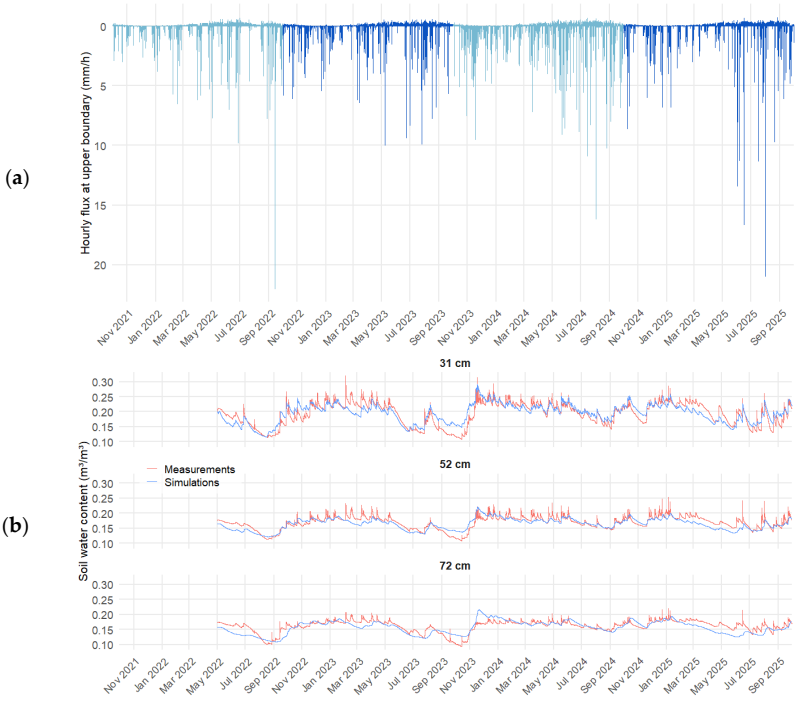


Figure 4. (**a**) Time series of hourly upper BC for the JP plot. This flux was obtained as the difference between rainfall and AET; the alternating colors allow distinguishing between different hydrological years. (**b**) Time series of soil water content at three different depths (31, 52, and 72 cm, respectively); red solid lines represent measurements obtained using TDR probes, while blue solid lines represent simulated values.

Accordingly, the temporal evolution of soil WC was analyzed at depths of 31, 52, and 72 cm, as illustrated in Figure 4b. This figure shows that the years 2022 and 2023 experienced marked and prolonged soil drying episodes, whereas in 2025, several rainfall events in August contributed to soil moisture recharge.

Equation (8) was applied to the parameters provided in Table 2, derived from ROSETTA, in order to obtain θ_r and θ_s values adjusted to the stoniness level of the soil profile. Then, the Levenberg–Marquardt algorithm implemented in WaMoS-IPE-1D was run to optimize the three parameters K_{sat}, α, and n. Table 3 summarizes the best set of parameters obtained for each layer, noting that our investigations led us to retain discretization JP2 and calibration period no. 3.

Table 2. Parameters obtained with ROSETTA using only the granulometric fractions for the three tested configurations.

Config.	Layer 1.	K_{sat} ($cm.d^{-1}$)	θ_r ($cm^3.cm^{-3}$)	θ_s ($cm^3.cm^{-3}$)	α (cm^{-1})	n (−)
JP-1	0–40	36.42	0.046	0.407	0.006	1.613
	40–75	28.94	0.046	0.403	0.007	1.576
	75–110	28.21	0.056	0.425	0.004	1.693
JP-2	0–35	36.419	0.046	0.407	0.006	1.613
	35–65	26.756	0.043	0.398	0.010	1.552
	65–110	29.598	0.005	0.420	0.005	1.682
HET-1	0–25	18.356	0.065	0.403	0.005	1.668
	25–45	23.378	0.061	0.437	0.004	1.692
	45–100	35.370	0.054	0.446	0.004	1.714

Table 3. Optimized MvG parameters for the JP soil profile, obtained with WaMoS-IPE-1D during calibration period no. 3. The KGE and NSE criteria were computed over each calibration period and also for the entire simulation period for which data were available.

Config.	Layer Min–Max Depth (cm)	K_{sat} ($cm.d^{-1}$)	θ_r ($cm^3.cm^{-3}$)	θ_s ($cm^3.cm^{-3}$)	α (cm^{-1})	n (–)	KGE (–)	NSE (–)
JP2-3	0–35	110.755	0.0461	0.4074	0.0064	1.6530	0.76	0.68
	35–65	28.957	0.0384	0.358	0.0089	1.5329	0.75	0.55
	65–110	28.853	0.0036	0.336	0.0043	1.6483	0.69	0.31
Global	All depths						0.83	0.67

3.3. Results at HET Plot

Figure 5a,b shows the temporal evolution of the surface flux and of the soil WC at three depths (20, 30, and 50 cm) for the beech plot (HET). The descriptions are broadly similar to those provided for the spruce plot (JP). It is worth noting that sensor data could be reliably exploited starting from May 2023, although a few interruptions occurred thereafter. For this HET plot, the proportion of AET was approximately 10% lower than that observed for the spruce plot during spring, while the relative contribution during summer was slightly higher. The soil WC curves indicate that the spring and summer of 2023 (calendar year) corresponded to the most pronounced soil drying period while the spring and summer of 2024 (calendar year) were the wettest recorded.

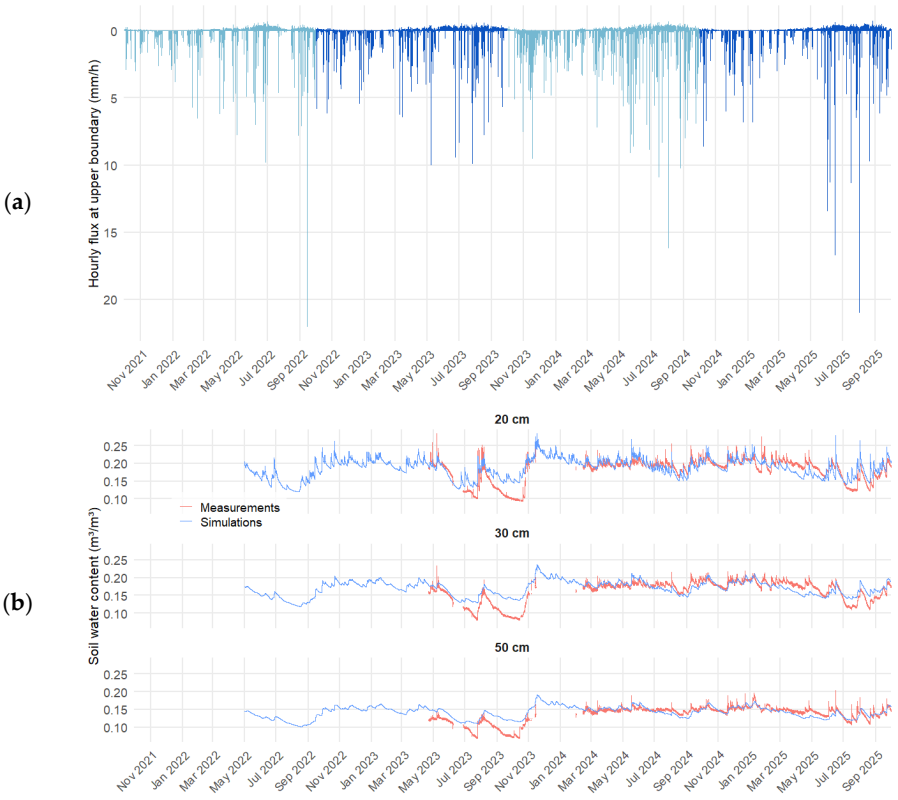


Figure 5. (**a**) Time series of hourly upper BC for the HET plot. This flux was obtained as the difference between rainfall and AET; the alternating colors allow distinguishing between different hydrological years. (**b**) Time series of soil water content at three different depths (20, 30, and 50 cm, respectively); red solid lines represent measurements obtained using SoilVue10 probe, while blue solid lines represent simulated values.

Following the same procedure as for the JP plot, the results obtained for the HET stand are presented in Table 4. The best set of parameters corresponded to calibration period no. 4.

Table 4. Optimized MvG parameters for the HET soil profile, obtained with WaMoS-IPE-1D during calibration period no. 4. The NSE criterion was computed over the entire simulation period for which data were available.

Config.	Layer Min–Max Depth (cm)	K_{sat} ($cm.d^{-1}$)	θ_s ($cm^3.cm^{-3}$)	θ_r ($cm^3.cm^{-3}$)	α (cm^{-1})	n (–)	KGE (–)	NSE (–)
HET1-4	0–25	19.684	0.3872	0.0581	0.0050	1.6982	0.60	0.54
	25–45	40.9050	0.3498	0.0487	0.0045	1.7085	0.50	0.51
	45–100	27.46861	0.2675	0.0322	0.0039	1.6472	0.51	0.48
Global	All depths						0.69	0.65

3.4. Analysis of Selected Calibration Periods, Efficiency Criterion and Estimated Parameters

All results dealing with estimated parameter sets and efficiency criterion are provided in the Supplementary Materials (Sections S3 and S4, respectively). To ensure transparency, all individual KGE and NSE values are reported for each layer and at the global scale, together with a radar-plot representation. The optimal configuration retained for the JP plot (i.e., JP2-3) was obtained from calibration during period 3; except for layer 2, the efficiency indices were higher than those from the other configurations. For the HET plot, calibration period 4 (HET1-4) yielded the selected optimal parameter set. This configuration produced the best NSE values and offered the most balanced performance. In contrast, configuration 2 achieved the highest KGE values but the lowest NSE scores, leading us to discard it.

Calibration period 4 was the longest, with an average of 8700 available measurements (across all three layers), whereas period 3 contained about 25% fewer data points. For the spruce plot, period 1 was the shortest and had the fewest soil moisture measurements. In the beech stand, period 1 contained no usable data, and period 2 was both the shortest and the least data-rich. These two calibration periods also exhibited the lowest average and minimum soil moisture values.

For the JP plot, the average soil moisture contents during calibration periods 3 and 4 were generally similar, while for the HET plot, they were slightly lower in 2025 than in 2024. In both plots, however, the 2024 hydrological year (calibration period 4) was characterized by lower minimum soil moisture values. The choice of calibration period therefore differed between the two plots. For the beech stand, the parameter sets HET1-4 and HET1-3 were relatively similar, whereas the set derived from calibration period 2 showed markedly different—and less efficient—parameter values. This discrepancy may be explained by particular environmental conditions or by reduced sensor reliability during that period, possibly due to imperfect contact between the sensor and the soil. The difficulty in accurately capturing the soil profile drying dynamics during the most intense episodes is likely due to the model applying transpiration only at the surface, whereas root water uptake should be represented over a root zone extending several tens of centimeters for both stands. In the Supplementary Materials, Figure S9 shows the soil WC time series obtained with the HET1-2 model, which provided a better fit during the 2023 drying season but was no longer suitable for the rest of the simulation. For the JP plot, the efficiency differences were more pronounced, making the choice of calibration period clearer. As with the beech stand, calibration period 2 resulted in a parameter set that was more distinct from the others, particularly regarding the properties of the successive soil layers.

Furthermore, this study shows that direct simulations using parameter sets derived from PTFs (e.g., ROSETTA) led to generally poorer performance, with KGE values of 0.74

for the JP plot and 0.26 for the HET plot, and NSE values of 0.15 and −2.75, respectively. This trend also holds when each soil layer is considered individually.

Undisturbed core sampling also enables the estimation of saturated hydraulic conductivity. At the JP plot, the measured values were consistent with the estimates obtained using WAMOS-IPE-1D: we indeed observed higher conductivity in the first layer that contained the surface horizon, and an overall lower conductivity below ~40 cm. The laboratory measurements suggest that a deeper layer with increased conductivity (just above the fractured zone) may exist, but this did not appear in the inversion due to the discretization chosen and the use of a thicker aggregated 3rd layer. For the beech stand, similarly, the model estimation supports the laboratory results, with an intermediate layer that was more conductive [35]. In accordance with previous discussions in [22], the parameters derived from the laboratory water retention curves tended to overestimate the retention capacity (θ_s–θ_r) of the soil system compared to parameters obtained from inverse modeling approach.

4. Discussion

As already mentioned and highlighted in [22], the proposed methodology focuses on optimizing only three key parameters (K_{sat}, α and n) of the soil constitutive relationships. To reduce the degrees of freedom of the inverse problem, the residual and saturated water contents (θ_r and θ_s, resp.) are assigned fixed values. While calibration using field data remains relatively scarce and requires additional supporting information [52], this approach is rather common in laboratory studies [53,54]. In accordance with recent contributions emphasizing multi-scale and depth-resolved evaluation of soil moisture dynamics (e.g., [55]), the choice of computing the performance metrics both layer-wise and globally was adopted to better reflect inter-layer variability and avoid overly aggregated interpretations. Identifying parameter sets that are simultaneously optimal at both the global scale profile and for each individual layer is challenging, due to potential compensatory effects among flow processes in the different layers and, possibly, equifinality issues. Furthermore, the performance metrics are not always consistent across criteria. Such discrepancies are well-documented in the literature (e.g., [50,56]), demonstrating that NSE and KGE are sensitive to different aspects of model behavior, and thus should not be interpreted interchangeably or uncritically. The findings of this study highlight the need for caution when implementing an inversion technique. As reported by [57], model efficiency scores should be used diagnostically to infer structural model behavior rather than as absolute performance numbers. As an illustration of this limitation, some of the relatively high KGE values reported in our results may occur even when the dynamic soil-moisture behavior is not reproduced accurately, underscoring the importance of interpreting performance metrics in light of the underlying hydrological processes (see [50]).

Regarding the selection of the calibration period, our analysis supports the conclusions of [58], who emphasized the importance of considering both wet and dry conditions over a sufficiently long time span when estimating parameters based on soil moisture data. This study also reinforces the critical role of a subsequent validation step to ensure the robustness of the calibration results.

In the site and measurements description (Section 2.3), it was noted that the mean particle-size distribution of the soil layers was established differently between the two plots: co-located with the sensors at JP with only one sample per layer, and derived from an average over five profiles for HET, and not taken precisely at the SoilVue10 installation location. This likely contributed to some uncertainty in the granulometric estimations, particularly for the HET stand, and perhaps to slightly weaker model performance.

The inverted van Genuchten parameters were benchmarked against the class means reported by [59]. Particle size distribution analysis classified the soil of plot JP as loam and

plot HET as sandy loam (in the USDA textural classification). As expected, the saturated water content (θ_s) was lower than the expected values, particularly in HET's third layer, probably due to the presence of stones and gravels. While some parameters (notably n and K_{sat} for certain layers) fell within or near expected ranges, the fitted α values were systematically lower than the means indicated by [59], and the residual water content (θ_r) for JP's third layer was notably low. These discrepancies likely reflect site-specific effects, such as stoniness and compaction. Comparison with parameters from other forest soils in the literature [32] indicates that the low α values are consistent with clayey soils. However, similar α values have also been reported for sandy or silt loam profiles. The remaining parameters, θ_s and n, align well with the ranges reported for these soil types. These results are generally reassuring, though it must be acknowledged that the measurement technique using sand/Kaolin box and small samples may introduce variability compared to our inversion approach based on in situ measurements. In addition, even when considered undisturbed, core samples may still yield a biased representation of coarse fragments and textural variations due to the dimensions of the sampling apparatus. Fundamentally, the low α values suggest finer particles and narrow pores, which appears contradictory to the increased presence of gravel and potential macroporosity at depth. This discrepancy may arise if the coarse fragments do not form a connected macropore network, or if weathering-derived fines have progressively filled voids between fragments. Such effects would lead to a predominantly microporous matrix despite the presence of coarse material.

The present study suggests that methodological differences between laboratory-based parameter estimation and inverse modeling using in situ sensors may contribute to the observed variability in results, particularly in stony soils. In practice, our approach must be adapted to the presence of coarse fragments. Even when introducing an additional degree of freedom and including the estimation of the saturated water content (θ_s), the inversion results do not significantly improve model performance, indicating that the stoniness-correction applied to the PTF-derived parameters, combined with inverse parameter estimation, remains a valuable approach to account for coarse fragments. There are still relatively few studies on forest soils applying comparable inversion-based approaches, which further emphasizes the need for caution and contextual interpretation.

5. Conclusions

Two forest plots of the Hydro Geochemical Environment Observatory in France, respectively composed of spruce (JP) and beech (HET), have been monitored for several years with soil water content sensors. However, the hydrodynamic parameters of the MvG model had not yet been determined for these stands. A methodology—that combines PFTs and inverse modeling approaches and includes stoniness—was therefore proposed and applied to optimize, for each plot, the set of parameters to be used in the Richards flow equation (Equation (7)). The study provides practical guidance for future modeling efforts in similar forested catchments. Specifically:

- Regarding calibration period selection: When calibration is performed over a limited time period, it is essential to assess the robustness of the selected parameter set over an extended period. In general, multi-period calibration is recommended, as it improves parameter transferability and model resilience under contrasting hydrological conditions. However, in strongly data-limited configurations, calibration using time periods that include a balanced range of moisture conditions (neither the driest nor the wettest period) may yield better performance. Conventional performance criteria should also be interpreted with caution, as they are not always consistent with one another.
- Concerning ROSETTA and PTF applications: ROSETTA remains an acceptable first guess when calibration data are scarce, but it should ideally be supplemented with

site-specific corrections or ancillary soil information. Accounting for the presence of stones and gravel to correct conductivity and water content has shown clear benefits in properly simulating water content time series, confirming findings from earlier studies on the subject [42,43]. Additionally, other PTFs better suited to European soils (see [60]), as well as integration of complementary information such as bulk density or field capacity, could further enhance model reliability.

- Regarding parameter identifiability from inverse modeling: Our calibration targeted three parameters: α, K_{sat}, and n. It appears that including the estimation of θ_s did not improve model performance when a stoniness correction had already been implemented.

Several approximations or modeling choices may impact these key findings and should be addressed in future work, the most notable being: (i) transpiration was obtained from pre-processing and applied at the soil surface rather than distributed over the rooting depth, (ii) preferential flow processes were not explicitly represented, despite stony soils being accounted for indirectly through parameter corrections, (iii) environmental boundary conditions (precipitation, AET) remain uncertain, and (iv) potential sensor–soil decoupling artifacts (particularly with the SoilVue10 sensor), as well as the lack of in situ calibration, may have influenced the measurements.

Nonetheless, hydrological simulations for the Strengbach catchment will benefit from this first hydrodynamic characterization of contrasting forest stands. The insights presented here provide a basis for implementing more mechanistic models that couple soil–plant hydraulics, energy balance, and photosynthesis [61], and suggest the possibility of addressing issues related to stand functioning.

Supplementary Materials: The following supporting information can be downloaded at https://www.mdpi.com/article/10.3390/hydrology13010011/s1. SI includes: Figure S1: Evolution of average monthly precipitation (blue line) and its variability (shaded areas) over the period from October 2007 to September 2025. The specific monthly values for the selected calibration periods are shown as colored dots; Figure S2: Evolution of average monthly temperature (red line) and its variability (shaded areas) over the period from October 2007 to September 2025. The specific monthly values for the selected calibration periods are shown as colored dots; Table S1: Parameters implemented in the BILHYDAY model for the spruce (JP) and beech (HET) plots obtained from prior studies and site-specific measurements; Figure S3: Seasonal evolution of cumulative AET for the spruce (JP, shown in red) and beech (HET, shown in green) plots at the Strengbach catchment; Figure S4: Graphical representation of the numerical methodology; Table S2: Parameters obtained for the spruce plot throughout the various tech-niques. Index i (1 to 3) refers to the soil layer: 1 = 0–35 cm, 2 = 35–65 cm, 3 = 65–110 cm; Figure S5: Hydrodynamic parameters obtained using different estimation techniques for the JP plot. Symbols represent the three soil layers, and colors distinguish the techniques. (a) representation of n vs. α; (b) representation of log(Ks) vs. (θ_s–θ_r); Table S3: Parameters obtained for the beech plot throughout the various techniques. Index i (1 to 3) refers to the soil layer: 1 = 0–25 cm, 2 = 25–45 cm, 3 = 45–100 cm; Figure S6: Hydrodynamic parameters obtained using different estimation techniques for the HET plot. Symbols represent the three soil layers, and colors distinguish the techniques. (a) representation of n vs. α with a zoomed-in window; (b) representation of log(Ks) vs. (θ_s–θ_r); Table S4: Efficiency criterion for the different configurations investigated on the spruce plot (JP); Figure S7: Radar charts illustrating the efficiency of the various estimation techniques applied to the JP plot. (a) shows the results for the complete profile; (b) for the first layer; (c) for the second layer; and (d) for the third layer; Table S5: Efficiency criterion for the different configurations investigated on the beech plot (HET); Figure S8: Radar charts illustrating the efficiency of the various estimation techniques applied to the HET plot. (a) shows the results for the complete profile; (b) for the first layer; (c) for the second layer; and (d) for the third layer; Figure S9: Comparison of soil water content (WC) time series obtained from the model (run

with the HET1-2 configuration; red line) and from measurements (blue line) for three soil layers at 31, 52, and 72 cm depth.

Author Contributions: B.B. conceptualization, software, supervision. A.A. and B.B.: methodology, simulation, validation. B.B., S.C. and A.J.: data acquisition and curation. A.A., B.B. and S.W.: writing—original draft preparation. A.A., B.B., S.C., A.J. and S.W.: writing—review and editing. All authors have read and agreed to the published version of the manuscript.

Funding: This research did not receive any direct external funding.

Data Availability Statement: Data concerning soil moisture are not yet available online. It can be requested from the corresponding author. Nevertheless, weather data are available on the BDOH platform: https://bd-ohge.unistra.fr/OHGE/ (accessed on 10 March 2025).

Acknowledgments: The authors are grateful to Strasbourg University, the National School for Water and Environmental Engineering of Strasbourg (ENGEES), and the Centre National de la Recherche Scientifique (CNRS) for supporting their research within their laboratory ITES-UMR7063. The authors would also like to thank the entire team at the Observatoire Hydro-Géochimique de l'Environnement for monitoring the field equipment, sampling the various compartments, conducting laboratory analyses, and managing and coordinating this site.

Conflicts of Interest: The authors declare no conflicts of interest. The funders had no role in the design of the study; in the collection, analyses, or interpretation of data; in the writing of the manuscript; or in the decision to publish the results.

Abbreviations

The following abbreviations are used in this manuscript:

AET	Actual evapotranspiration
BC	Boundary condition(s)
BILHYDAY	Daily water mass balance model
CC	Climate change
HET	Beech plot in the Strengbach catchment (stands for Hêtraie in French)
JP	Young Norway spruce plot in the Strengbach catchment (stands for Jeune Peuplement in French)
KGE	Kling-Gupta efficiency criterion
LAI	Leaf area index
MvG	Mualem-van Genuchten hydrodynamic model
NSE	Nash–Sutcliffe efficiency criterion
OHGE	Observatoire Hydro-Géochimique de l'Environnement (https://ohge.unistra.fr/)
PET	Potential evapotranspiration
PTFs	Pedotransfer functions
RE	Richards' Equation
TDR	Time-Domain Reflectometry
WaMoS-IPE-1D	Water movement in soil–inverse parameters estimation–1-dimensional
WC	Water content

References

1. Aznar-Sánchez, J.A.; Belmonte-Ureña, L.J.; López-Serrano, M.J.; Velasco-Muñoz, J.F. Forest Ecosystem Services: An Analysis of Worldwide Research. *Forests* **2018**, *9*, 453. [CrossRef]
2. Nolander, C.; Lundmark, R. A Review of Forest Ecosystem Services and Their Spatial Value Characteristics. *Forests* **2024**, *15*, 919. [CrossRef]
3. FAO. *The State of the World's Forests 2024*; FAO: Rome, Italy, 2024; ISBN 978-92-5-138867-9.
4. Forzieri, G.; Dakos, V.; McDowell, N.G.; Ramdane, A.; Cescatti, A. Emerging Signals of Declining Forest Resilience under Climate Change. *Nature* **2022**, *608*, 534–539. [CrossRef]

5. Hammond, W.M.; Williams, A.P.; Abatzoglou, J.T.; Adams, H.D.; Klein, T.; López, R.; Sáenz-Romero, C.; Hartmann, H.; Breshears, D.D.; Allen, C.D. Global Field Observations of Tree Die-off Reveal Hotter-Drought Fingerprint for Earth's Forests. *Nat. Commun.* **2022**, *13*, 1761. [CrossRef] [PubMed]
6. Hlásny, T.; Zimová, S.; Merganičová, K.; Štěpánek, P.; Modlinger, R.; Turčáni, M. Devastating Outbreak of Bark Beetles in the Czech Republic: Drivers, Impacts, and Management Implications. *For. Ecol. Manag.* **2021**, *490*, 119075. [CrossRef]
7. Richardson, D.; Black, A.S.; Irving, D.; Matear, R.J.; Monselesan, D.P.; Risbey, J.S.; Squire, D.T.; Tozer, C.R. Global Increase in Wildfire Potential from Compound Fire Weather and Drought. *npj Clim. Atmos. Sci.* **2022**, *5*, 23. [CrossRef]
8. Tromp-van Meerveld, H.J.; McDonnell, J.J. On the Interrelations between Topography, Soil Depth, Soil Moisture, Transpiration Rates and Species Distribution at the Hillslope Scale. *Adv. Water Resour.* **2006**, *29*, 293–310. [CrossRef]
9. Sabater, A.M.; Valiente, J.A.; Bellot, J.; Vilagrosa, A. Climatic Factors Influencing Aleppo Pine Sap Flow in Orographic Valleys Under Two Contrasting Mediterranean Climates. *Hydrology* **2025**, *12*, 6. [CrossRef]
10. Vorobevskii, I.; Luong, T.T.; Kronenberg, R.; Petzold, R. High-Resolution Operational Soil Moisture Monitoring for Forests in Central Germany. *Hydrol. Earth Syst. Sci.* **2024**, *28*, 3567–3595. [CrossRef]
11. Singh, A.; Gaurav, K. Deep Learning and Data Fusion to Estimate Surface Soil Moisture from Multi-Sensor Satellite Images. *Sci. Rep.* **2023**, *13*, 2251. [CrossRef] [PubMed]
12. Cosh, M.H.; Caldwell, T.G.; Baker, C.B.; Bolten, J.D.; Edwards, N.; Goble, P.; Hofman, H.; Ochsner, T.E.; Quiring, S.; Schalk, C.; et al. Developing a Strategy for the National Coordinated Soil Moisture Monitoring Network. *Vadose Zone J.* **2021**, *20*, e20139. [CrossRef]
13. Braud, I.; Chaffard, V.; Coussot, C.; Galle, S.; Juen, P.; Alexandre, H.; Baillion, P.; Battais, A.; Boudevillain, B.; Branger, F.; et al. Building the Information System of the French Critical Zone Observatories Network: Theia/OZCAR-IS. *Hydrol. Sci. J.* **2022**, *67*, 2401–2419. [CrossRef]
14. Meyer, S.; Blaschek, M.; Duttmann, R.; Ludwig, R. Improved Hydrological Model Parametrization for Climate Change Impact Assessment under Data Scarcity—The Potential of Field Monitoring Techniques and Geostatistics. *Sci. Total Environ.* **2016**, *543*, 906–923. [CrossRef]
15. Koohbor, B.; Fahs, M.; Hoteit, H.; Doummar, J.; Younes, A.; Belfort, B. An Advanced Discrete Fracture Model for Variably Saturated Flow in Fractured Porous Media. *Adv. Water Resour.* **2020**, *140*, 103602. [CrossRef]
16. Camporese, M.; Daly, E.; Paniconi, C. Catchment-Scale Richards Equation-Based Modeling of Evapotranspiration via Boundary Condition Switching and Root Water Uptake Schemes. *Water Resour. Res.* **2015**, *51*, 5756–5771. [CrossRef]
17. Chaguer, M.; Weill, S.; Ackerer, P.; Delay, F. Implementation of Subsurface Transport Processes in the Low-Dimensional Integrated Hydrological Model NIHM. *J. Hydrol.* **2022**, *609*, 127696. [CrossRef]
18. Schaap, M.G.; Leij, F.J.; Van Genuchten, M.T. Rosetta: A Computer Program for Estimating Soil Hydraulic Parameters with Hierarchical Pedotransfer Functions. *J. Hydrol.* **2001**, *251*, 163–176. [CrossRef]
19. Graham, S.L.; Srinivasan, M.S.; Faulkner, N.; Carrick, S. Soil Hydraulic Modeling Outcomes with Four Parameterization Methods: Comparing Soil Description and Inverse Estimation Approaches. *Vadose Zone J.* **2018**, *17*, 170002. [CrossRef]
20. Lesparre, N.; Pasquet, S.; Ackerer, P. Impacts of Hydrofacies Geometry Designed from Seismic Refraction Tomography on Estimated Hydrogeophysical Variables. *Hydrol. Earth Syst. Sci.* **2024**, *28*, 873–897. [CrossRef]
21. Moua, R.; Lesparre, N.; Girard, J.-F.; Belfort, B.; Lehmann, F.; Younes, A. Coupled Hydrogeophysical Inversion of an Artificial Infiltration Experiment Monitored with Ground-Penetrating Radar: Synthetic Demonstration. *Hydrol. Earth Syst. Sci.* **2023**, *27*, 4317–4334. [CrossRef]
22. Belfort, B.; Toloni, I.; Ackerer, P.; Cotel, S.; Viville, D.; Lehmann, F. Vadose Zone Modeling in a Small Forested Catchment: Impact of Water Pressure Head Sampling Frequency on 1D-Model Calibration. *Geosciences* **2018**, *8*, 72. [CrossRef]
23. Novák, V.; Kňava, K. The Influence of Stoniness and Canopy Properties on Soil Water Content Distribution: Simulation of Water Movement in Forest Stony Soil. *Eur. J. For. Res.* **2012**, *131*, 1727–1735. [CrossRef]
24. Naseri, M.; Joshi, D.C.; Iden, S.C.; Durner, W. Rock Fragments Influence the Water Retention and Hydraulic Conductivity of Soils. *Vadose Zone J.* **2023**, *22*, e20243. [CrossRef]
25. Pierret, M.-C.; Cotel, S.; Ackerer, P.; Beaulieu, E.; Benarioumlil, S.; Boucher, M.; Boutin, R.; Chabaux, F.; Delay, F.; Fourtet, C.; et al. The Strengbach Catchment: A Multidisciplinary Environmental Sentry for 30 Years. *Vadose Zone J.* **2018**, *17*, 180090. [CrossRef]
26. Beaulieu, E.; Pierret, M.-C.; Legout, A.; Chabaux, F.; Goddéris, Y.; Viville, D.; Herrmann, A. Response of a Forested Catchment over the Last 25 Years to Past Acid Deposition Assessed by Biogeochemical Cycle Modeling (Strengbach, France). *Ecol. Model.* **2020**, *430*, 109124. [CrossRef]
27. Oursin, M.; Pierret, M.-C.; Beaulieu, É.; Daval, D.; Legout, A. Is There Still Something to Eat for Trees in the Soils of the Strengbach Catchment? *For. Ecol. Manag.* **2023**, *527*, 120583. [CrossRef]
28. Strohmenger, L.; Ackerer, P.; Belfort, B.; Pierret, M.C. Local and Seasonal Climate Change and Its Influence on the Hydrological Cycle in a Mountainous Forested Catchment. *J. Hydrol.* **2022**, *610*, 127914. [CrossRef]

29. Ackerer, J.; Jeannot, B.; Delay, F.; Weill, S.; Lucas, Y.; Fritz, B.; Viville, D.; Chabaux, F. Crossing Hydrological and Geochemical Modeling to Understand the Spatiotemporal Variability of Water Chemistry in a Headwater Catchment (Strengbach, France). *Hydrol. Earth Syst. Sci.* **2020**, *24*, 3111–3133. [CrossRef]
30. Weill, S.; Lesparre, N.; Jeannot, B.; Delay, F. Variability of Water Transit Time Distributions at the Strengbach Catchment (Vosges Mountains, France) Inferred Through Integrated Hydrological Modeling and Particle Tracking Algorithms. *Water* **2019**, *11*, 2637. [CrossRef]
31. Lesparre, N.; Girard, J.-F.; Jeannot, B.; Weill, S.; Dumont, M.; Boucher, M.; Viville, D.; Pierret, M.-C.; Legchenko, A.; Delay, F. Magnetic Resonance Sounding Dataset of a Hard-Rock Headwater Catchment for Assessing the Vertical Distribution of Water Contents in the Subsurface. *Data Brief* **2020**, *31*, 105708. [CrossRef] [PubMed]
32. De Vos, B.; Cools, N.; Verstraeten, A.; Neirynck, J. Accurate Measurements of Forest Soil Water Content Using FDR Sensors Require Empirical In Situ (Re)Calibration. *Appl. Sci.* **2021**, *11*, 11620. [CrossRef]
33. Dong, Y.; Miller, S.; Kelley, L. Performance Evaluation of Soil Moisture Sensors in Coarse- and Fine-Textured Michigan Agricultural Soils. *Agriculture* **2020**, *10*, 598. [CrossRef]
34. Thakur, V.; Markonis, Y.; Kumar, R.; Thomson, J.R.; Vargas Godoy, M.R.; Hanel, M.; Rakovec, O. Unveiling the Impact of Potential Evapotranspiration Method Selection on Trends in Hydrological Cycle Components across Europe. *Hydrol. Earth Syst. Sci.* **2025**, *29*, 4395–4416. [CrossRef]
35. Biron, P. Le Cycle de l'eau En Forêt de Moyenne Montagne: Flux de Sêve et Bilans Hydriques Stationnels: Bassin Versant Du Strengbach à Aubure, Hautes Vosges. Ph.D. Thesis, Université Louis Pasteur (1971–2008), Strasbourg, France, 1994.
36. Brochet, P.; Gerbier, N. *L'Evapotranspiration: Aspect Agrométéorologique, Evaluation Pratique de l'Evapotranspiration Potentielle*; Monographie n°65 de la Météorologie nationale; Edition revue et complétée; Edition revue et complétée; Direction de la Météorologie Nationale: Paris, France, 1975.
37. Granier, A.; Bréda, N.; Biron, P.; Villette, S. A Lumped Water Balance Model to Evaluate Duration and Intensity of Drought Constraints in Forest Stands. *Ecol. Model.* **1999**, *116*, 269–283. [CrossRef]
38. Viville, D.; Biron, P.; Granier, A.; Dambrine, E.; Probst, A. Interception in a Mountainous Declining Spruce Stand in the Strengbach Catchment (Vosges, France). *J. Hydrol.* **1993**, *144*, 273–282. [CrossRef]
39. Richards, L.A. Capillary Conduction of Liquids through Porous Mediums. *Physics* **1931**, *1*, 318–333. [CrossRef]
40. Van Genuchten, M.T. A Closed-Form Equation for Predicting the Hydraulic Conductivity of Unsaturated Soils. *Soil Sci. Soc. Am. J.* **1980**, *44*, 892–898. [CrossRef]
41. Mualem, Y. A New Model for Predicting the Hydraulic Conductivity of Unsaturated Porous Media. *Water Resour. Res.* **1976**, *12*, 513–522. [CrossRef]
42. Bouwer, H.; Rice, R.C. Hydraulic Properties of Stony Vadose Zones. *Groundwater* **1984**, *22*, 696–705. [CrossRef]
43. Hlaváčiková, H.; Novák, V.; Holko, L. On the Role of Rock Fragments and Initial Soil Water Content in the Potential Subsurface Runoff Formation. *J. Hydrol. Hydromech.* **2015**, *63*, 71–81. [CrossRef]
44. Lehmann, F.; Ackerer, P. Comparison of Iterative Methods for Improved Solutions of the Fluid Flow Equation in Partially Saturated Porous Media. *Transp. Porous Media* **1998**, *31*, 275–292. [CrossRef]
45. Belfort, B.; Carrayrou, J.; Lehmann, F. Implementation of Richardson Extrapolation in an Efficient Adaptive Time Stepping Method: Applications to Reactive Transport and Unsaturated Flow in Porous Media. *Transp. Porous Media* **2007**, *69*, 123–138. [CrossRef]
46. van Dam, J.C.; Feddes, R.A. Numerical Simulation of Infiltration, Evaporation and Shallow Groundwater Levels with the Richards Equation. *J. Hydrol.* **2000**, *233*, 72–85. [CrossRef]
47. Marquardt, D.W. An Algorithm for Least-Squares Estimation of Nonlinear Parameters. *J. Soc. Ind. Appl. Math.* **1963**, *11*, 431–441. [CrossRef]
48. Lehmann, F.; Ackerer, P. Determining soil hydraulic properties by inverse method in one-dimensional unsaturated flow. *J. Environ. Qual.* **1997**, *26*, 76–81. [CrossRef]
49. Zhou, H.; Gómez-Hernández, J.J.; Li, L. Inverse Methods in Hydrogeology: Evolution and Recent Trends. *Adv. Water Resour.* **2014**, *63*, 22–37. [CrossRef]
50. Gupta, H.V.; Kling, H.; Yilmaz, K.K.; Martinez, G.F. Decomposition of the Mean Squared Error and NSE Performance Criteria: Implications for Improving Hydrological Modelling. *J. Hydrol.* **2009**, *377*, 80–91. [CrossRef]
51. Nash, J.E.; Sutcliffe, J.V. River Flow Forecasting through Conceptual Models Part I—A Discussion of Principles. *J. Hydrol.* **1970**, *10*, 282–290. [CrossRef]
52. Scharnagl, B.; Vrugt, J.A.; Vereecken, H.; Herbst, M. Inverse Modelling of in Situ Soil Water Dynamics: Investigating the Effect of Different Prior Distributions of the Soil Hydraulic Parameters. *Hydrol. Earth Syst. Sci.* **2011**, *15*, 3043–3059. [CrossRef]
53. Hajizadeh Javaran, M.R.; Rajabi, M.M.; Kamali, N.; Fahs, M.; Belfort, B. Encoder–Decoder Convolutional Neural Networks for Flow Modeling in Unsaturated Porous Media: Forward and Inverse Approaches. *Water* **2023**, *15*, 2890. [CrossRef]

54. Latorre, B.; Moret-Fernández, D. Simultaneous Estimation of the Soil Hydraulic Conductivity and the van Genuchten Water Retention Parameters from an Upward Infiltration Experiment. *J. Hydrol.* **2019**, *572*, 461–469. [CrossRef]
55. He, Y.; Mao, H.; Wang, C.; Hu, J.; Ninsawat, S.; Song, X.; Jing, G.; Li, R.; Wang, M.; Duan, Z. Advancing Hydrological Modeling through Multivariate Calibration of Multi-Layer Soil Moisture Dynamics. *J. Hydrol. Reg. Stud.* **2025**, *57*, 102125. [CrossRef]
56. Knoben, W.J.M.; Freer, J.E.; Woods, R.A. Technical Note: Inherent Benchmark or Not? Comparing Nash–Sutcliffe and Kling–Gupta Efficiency Scores. *Hydrol. Earth Syst. Sci.* **2019**, *23*, 4323–4331. [CrossRef]
57. Schwemmle, R.; Demand, D.; Weiler, M. Technical Note: Diagnostic Efficiency—Specific Evaluation of Model Performance. *Hydrol. Earth Syst. Sci.* **2021**, *25*, 2187–2198. [CrossRef]
58. Zhang, Z.F.; Ward, A.L.; Gee, G.W. Estimating Soil Hydraulic Parameters of a Field Drainage Experiment Using Inverse Techniques. *Vadose Zone J.* **2003**, *2*, 201–211. [CrossRef]
59. Carsel, R.F.; Parrish, R.S. Developing Joint Probability Distributions of Soil Water Retention Characteristics. *Water Resour. Res.* **1988**, *24*, 755–769. [CrossRef]
60. Tóth, B.; Weynants, M.; Nemes, A.; Makó, A.; Bilas, G.; Tóth, G. New Generation of Hydraulic Pedotransfer Functions for Europe. *Eur. J. Soil Sci.* **2015**, *66*, 226–238. [CrossRef]
61. Corvi, O. Développement d'un Nouveau Modèle à Base Physique de Représentation Du Continuum Sol-Plante-Atmosphère Incluant l'Hydraulique des Plantes. Ph.D. Thesis, Université de Strasbourg, Strasbourg, France, 27 May 2025.

Disclaimer/Publisher's Note: The statements, opinions and data contained in all publications are solely those of the individual author(s) and contributor(s) and not of MDPI and/or the editor(s). MDPI and/or the editor(s) disclaim responsibility for any injury to people or property resulting from any ideas, methods, instructions or products referred to in the content.